Nano Energy 74 (2020) 104874

Contents lists available at ScienceDirect

Nano Energy

journal homepage: http://www.elsevier.com/locate/nanoen

A theoretical modeling analysis for triboelectrification controlled light emitting diodes

Abdelsalam Ahmed [a,b,*], Mohamed Shehata [c], Islam Hassan [d], Yasmine I. Abdelhak [e], Efe Cigdem [f], Maher El-Kady [g,h], Yehea Ismail [i], Hassan Mostafa [j,i]

[a] Harvard Medical School, Harvard University, Boston, MA, 02115, United States
[b] Department of Mechanical Engineering, Massachusetts Institute of Technology, Cambridge, MA, 02139, United States
[c] School of Electrical and Electronic Engineering, The University of Adelaide, Adelaide, SA, 5005, Australia
[d] Department of Mechanical Engineering, McMaster University, Hamilton, ON, L8S 4L7, Canada
[e] Department of Electronics and Communications, Faculty of Engineering, Mansoura University, 35511, Dakahlia, Egypt
[f] Department of Electrical & Computer Engineering, University of Toronto, Toronto, ON, M5S 3G8, Canada
[g] Department of Materials Science and Engineering, UCLA, Los Angeles, CA, 90095, United States
[h] Department of Chemistry and Biochemistry and California NanoSystems Institute, University of California, Los Angeles (UCLA), Loss Angeles, CA, 90095, United States
[i] University of Science and Technology, Nanotechnology and Nanoelectronics Program, Zewail City of Science and Technology, October Gardens, 6th of October, Giza, 12578, Egypt
[j] Department of Electronics and Communications, Faculty of Engineering, Cairo University, 11432, Giza, Egypt

ARTICLE INFO

Keywords:
Tribo-phototronic
Design guidelines
Theoretical framework

ABSTRACT

In this paper, we demonstrate the use of triboelectric nanogenerator (TENG) as a mean of mechanical light triggering to control InGaN-based light-emitting diodes (LEDs). Light extraction from the LED is two successive steps process. First, the voltage produced by the TENG is used to control the gate-to-source current of a MOSFET transistor through adjusting the transistor channel width and length. The second step is forwarding the drain-source current resulting from MOSFET transistor to the LED as its injection current to induce spontaneous emission from the LED surface to the air. Three LED colors are considered: red, green and blue. Significant emitted power from these InGaN-based LEDs in the RGB wavelength band is observed for both P-MOSFET and N-MOSFET transistor configurations. The emitted optical spectrum is controlled by optimizing the combined TENG-MOSFET-RGB LED geometry; dimensions and the bias voltage between the drain and source terminals of the MOSFET transistor. With recent advances in TENGs as an energy harvesting technology, it is expected that this study offers an approach to enhance the light extraction of various LED devices. With the enhancements in the performance of optoelectronic devices, the field of tribo-phototronics has attracted more attention, and in this work, we introduce the first theoretical framework, to the best of our knowledge, based on finite element modeling. This study provides significant insights into the working principles of tribo-Phototronic devices as well as guidelines for future device design.

1. Introduction

Triboelectric nanogenerator (TENG) based energy harvesting technology has been extensively employed in a variety of engineering applications to empower electronic components and devices [1]. Since the first invented TENG has been introduced in 2012 [2–4], various applications based on this novel energy harvesting technology, have been proposed in this newly emerging field [5–14]. Tribotronics is a new field that uses the electrostatic potential created by mechanical energy as a control voltage to control current transport in semiconductor devices such as the gate voltage in metal oxide semiconductor field effect transistors (MOSFETs) [15–19]. Numerous fundamental electronic components, devices, and electronic circuits have been demonstrated.

A TENG, working in contact electrification (CE), has been utilized to empower a metal oxide semiconductor field effect transistor (MOSFET) by connecting the two output ports of a TENG to the gate-source terminals of the MOSFET transistor. Different designs have been developed for wearable applications [20–24]. The performance of the

* Corresponding author. Harvard Medical School, Harvard University, Boston, MA, 02115, United States.
E-mail address: aahmed26@bwh.harvard.edu (A. Ahmed).

https://doi.org/10.1016/j.nanoen.2020.104874
Received 11 February 2020; Received in revised form 19 April 2020; Accepted 20 April 2020
Available online 1 May 2020

aforementioned devices and systems has been demonstrated experimentally. Tribotronic-based devices have also been developed to perform basic logic operations such as the binary logic inversion as well as the OR, AND, NAND and NOR operations. Furthermore, new fields have also emerged by coupling the tribotronic technology with other existing fields. The radiative electron-hole recombination in light emitting diodes (LEDs) is widely used in a broad category of customer electronics such as TVs, screens, traffic lights … etc. [25–27] TENG empowered light emitting diodes (LEDs), and phototransistors are promising examples of emerging phototronic devices [28].

Although several TENG-based electronic systems have already been developed and experimentally demonstrated, accurate modeling of the TENG performance as a circuit element coupled to empower conventional electronic components and devices is still an open research niche that needs further investigations and explorations. A theoretical model for the impact of parasitic capacitance on the performance of TENGs has been presented. This paper provides some general guidelines to modeling, analysis, design as well as the performance characterization of TENG-based optoelectronic devices in order to maximize the overall power conversion efficiency. In this context, a TENG working in the contact-release mode is described and modeled.

In this paper, a fundamental theoretical framework of the tribo-phototronic devices is developed with the combination of contact-electrification gated transistors and optoelectronic devices. An enhanced equivalent circuit is introduced. The developed model quantifies the performance, of LEDs coupled to the TENG via a MOSFET

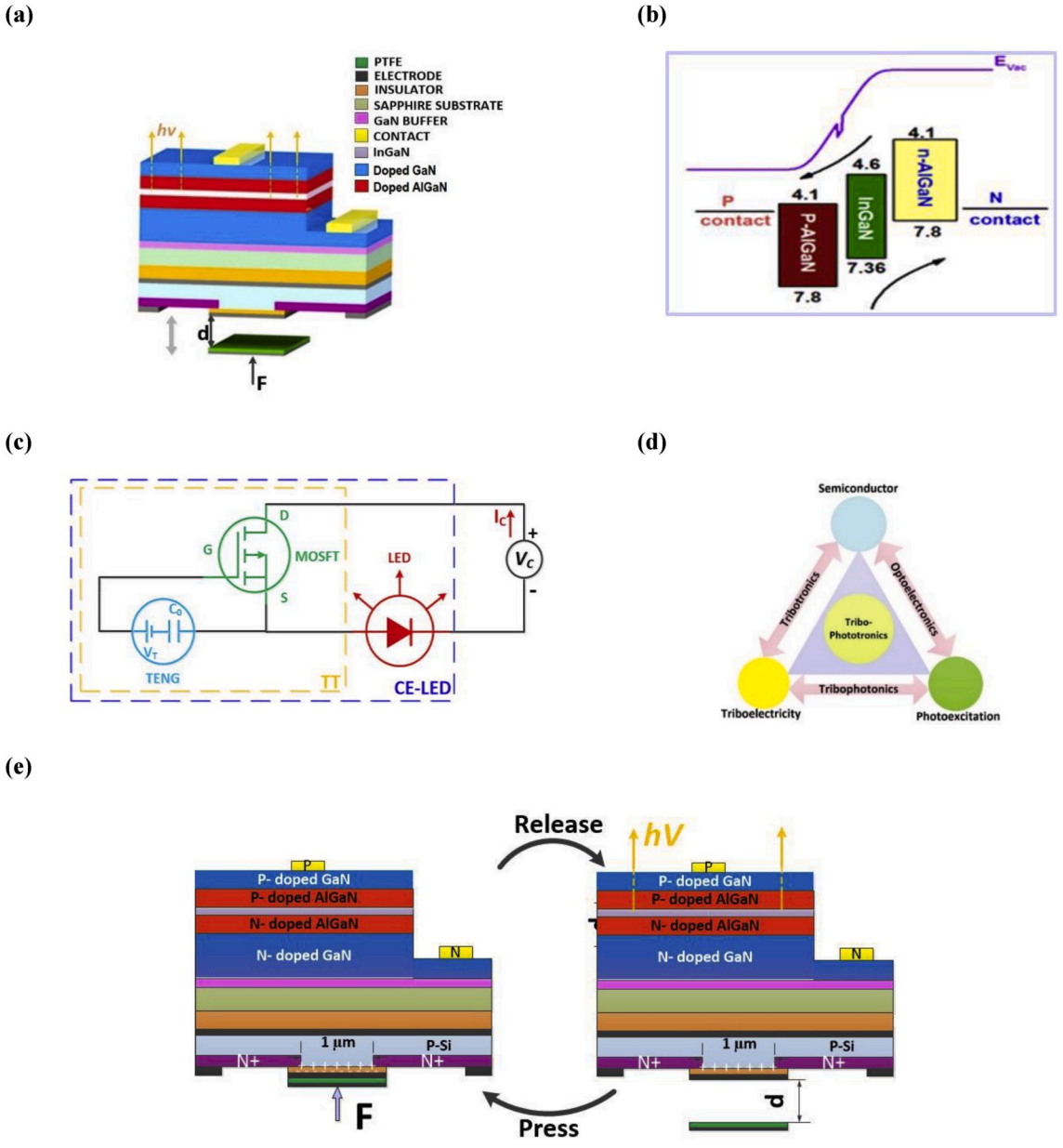

Fig. 1. **(a)** Device structure and geometry of the TENG controlled LED via a PTFE (polytetrafluoroethylene) layer-based MOSFET transistor that operating in the external bias mode **(b)** Bandgap diagram for LED under 0 V and 3.3 V biasing, **(c)** Schematic illustration of the contact-electrification-gated light-emitting diode (CE-LED). Structure of the CE-LED based on a light-emitting diode (LED), an organic thin film transistor (MOSFET), and a triboelectric nanogenerator (TENG) in vertical contact-separation mode, the equivalent circuit of the CE-LED. **(d)** Schematic diagram of multi-field coupling effect among physical quantities of semiconductor, photoexcitation, and triboelectricity including two coupling effects (optoelectronics, tribophototronics and Tribotronics) and three-way coupling effect Tribo-Photonics. **(e)** Principle and characteristics of the CE-LED with Schematic working principle of the CE-LED, the brightness is increased when the gap distance d is increased.

transistor. A MOSFET transistor interfacing the TENG-LED system is also studied through simulations. The critical operating parameters, that influence performance characteristics, are identified and carefully designed in order to improve the overall system performance. Moreover, the three different modes of MOSFET operation [29,30], coupled to the TENG and the LED, are analyzed in order to maximize the output optical power. In this study, these components have been analyzed in detail, and the best input combination for a specific output is presented. With this methodology/simulation, we utilize COMSOL Multiphysics software to analyze the performance of the proposed structure. The established theoretical workbench provides a suitable model for the development of tribo-phototronic-based effects and provides useful guidelines for future device design.

2. Results and discussion

The input-output (I/O) characteristics of each system component are individually analyzed by identifying its necessary and sufficient structural parameters as shown in Table S1 (see Supporting Information). These structural parameters are then controlled in order to maximize the output optical power. For the triboelectric part, the contact-separation mode of TENG is used, in this design, to provide a high output voltage at the TENG terminals. In TENG, we focused on the effect of the distance between the two triboelectric layers. The proposed device depends on an external biasing voltage source which provides a drain-source current gain. The voltage potential is only built at the Gate electrode which controls the amount of current flowing from one terminal to the other one. The second property that we studied is the external efficiency of the LED device to see in which region LED works most efficiently. Third property that we studied is emission rate-current graph to analyze how much current is needed to supply a specific amount of emission. The emission spectral density versus the emitted wavelength is also investigated. Fig. 1(a) depicts the architectural design and the equivalent schematic diagram of the TENG- MOSFET-LED configuration. The triboelectric nanogenerator is built vertically aligned with the MOSFET as depicted in Fig. 1(a). Fig. 1(b) provides schematic illustrations of the energy band alignment between charge transport layers with different band gaps and energy levels. The band edge positions are based on band energies relative to the vacuum level.

As shown in Fig. S1, a detailed schematic with all dimensions and structure layers is mentioned for the TENG-MOSFET-LED. Moreover, in the contact-electrification CE-LED, the tribotronic transistor (TT) and the LED are electrically connected in series with a voltage source. The equivalent circuit of the CE-LED is described as shown in Fig. 1(c). For the TT, the TENG provides a gate voltage to the MOSFET by applying a physical force for controlling the drain current. Therefore, the light-emission intensity of the CE-LED is modulated by the external force–induced contact electrification. Fig. 1(d) represents a map which describes the three-way interaction among physical quantities of the MOSFET as a semiconductor device, photo-excitation as an optical device and triboelectricity effects offered by the TENG.

Furthermore, the combination of two or more effects mentioned above can generate multi-field couplings as shown in Fig. 1(d). The working principle of the TT is based on the coupling effects of the MOSFET and the TENG with the vertical contact-separation mode, which is schematically shown in Fig. 1(e). When the external force is applied on the movable layer, the PTFE and electrode films are vertically contacted with each other for electrification, leaving net positive charges on the fixed electrode film and net negative charges on the PTFE film for the triboelectrification. The produced triboelectric charges with opposite polarities are fully balanced, and the gate voltage is zero at this moment. When the external force is released, the movable layer is separated from the fixed electrode film for a certain distance. The negative charges on the PTFE film induce the electrons flow from the movable electrode to the P–Si gate electrode to screen the electrostatic field. Due to the source electrode is connected to the fixed electrode film with positive charges, a negative gate voltage is applied on the gate electrode of the MOSFET, and the p-type conduction channel is widened, which increases the drain current. When the external force is applied and the movable layer contacts with the fixed electrode film again, the balance of the triboelectric charges cause the electrons flow back from the P–Si gate electrode to the movable electrode. The gate voltage turns back to zero, and the conduction channel is narrowed, which decreases the drain current to the initial state. Therefore, the drain current of the TT can be gated by the external force–induced contact electrification, by modulating the gap distance between the movable layer and the fixed electrode film, which as the same effect as the traditional gate voltage. Therefore, the gap distance is used as a controlling parameter in the following discussions. Throughout this paper, the framework of the proposed tribo-phototronic model is developed based on coupling the theories of semiconductors, triboelectricity, and optoelectronics. Numerical simulations, using the finite element method, confirm the validity of the theoretically obtained results.

The principle of operation of the TENG-MOSFET-LED configuration is described as follows. The TENG acts as a mechanical-to-electrical power transducer to control the output optical power of the LED through the MOSFET transistor. Here, the MOSFET transistor works as a current regulating element whose role is to control the output optical intensity via the Drain-Source current which can be controlled by the channel length modulation. This current is the LED photo-excitation current. The MOSFET structural parameters which influence its performance are investigated. All the governing equations and MOSFET modes of operations can be found at Supplementary Note 1 (see Supporting Information).

The total list of inputs can be found in Table S1. Our study analyzes the relationship of the distance between the contact materials to the potential created at the gate-source terminals of the MOSFET transistor. The gap distance between the contact materials is increased from 0.5 μm to 3 μm and the corresponding potential difference at the TENG terminals is observed. According to Fig. 2, the maximum gate voltage is achieved at the maximum electrode separation of $d = 3$ μm as expected. At this point, the gate voltage drives the Gate-Source terminals of the MOSFET transistor. Currently, three types of LEDs are built in this study. In order to analyze the material properties under the same circumstances and analyze the properties in 3 different aspects: Current vs. Voltage, External Quantum Efficiency, and Total Emission Rate vs. Current. The I–V characteristics of the LED is given by two types of MOSFET transistors (PMOS and NMOS) are considered in order to analyze the performance of the electrons and holes. Moreover, the impact of the Drain-Source channel length between the source and the drain terminals on the flow of Source-Drain current is investigated. The impact of the D-S channel length is found to balance between the amount of current flowing and the threshold voltage, which is the required voltage to turn ON the MOSFET transistor. The second parameter that we discuss is the doping concentrations effect on the MOSFET output current, which is used to control the output optical power of the LED component.

We build two simulations: In the first simulation, we kept the body concentration constant and changed the drain/source concentrations. In the second simulation, the drain/source concentrations are fixed, and the body concentration is varied. The impact of doping concentrations on the output current is also analyzed in these simulations. The third parameter that we discuss is the metal-semiconductor contact type's effect on the output current. There are two types of contacts: Ohmic and Schottky. Schottky type of contact builds a diode behavior at the contact, whereas, Ohmic contact acts as a resistor. The fourth parameter is the gate oxide thickness effects on the current output. Various thickness parameters are simulated in NMOS and PMOS transistors, and the results are observed. It affects the balance between the amount of current flowing and the threshold voltage. The last parameter is the drain and gate voltage effects on current output. This study contains different sets of data for MOS types and TENG modes of operations since gate and

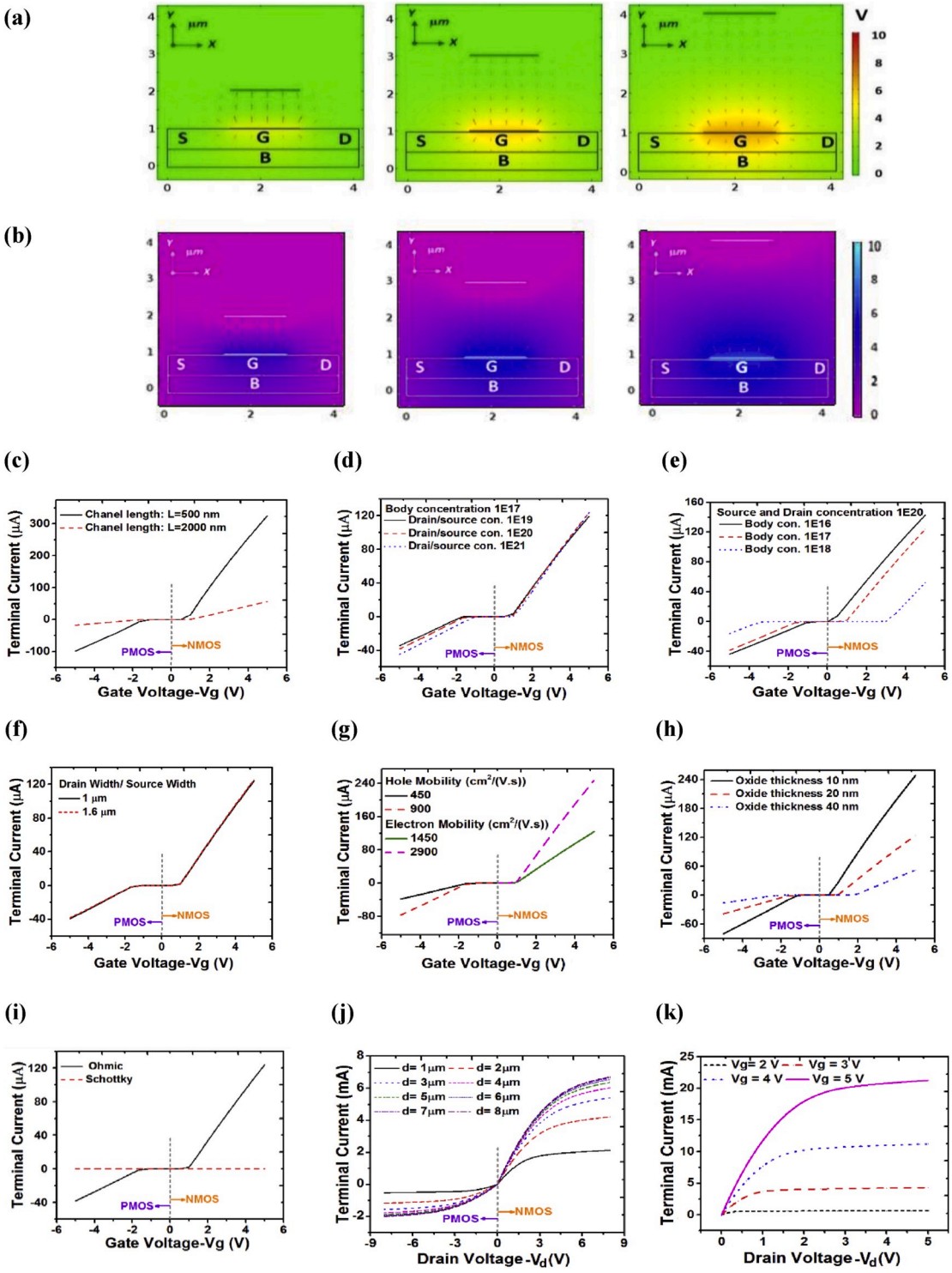

Fig. 2. Spatial distribution of the potential across the gate layer under varying contact distance for **(a)** NMOS and **(b)** PMOS transistor types. Terminal drain-source current versus the gate/TENG voltage V_g for both NMOS and PMOS transistor types at various **(c)** Drain-to-source channel lengths, **(d)** Source and drain concentrations, **(e)** Body concentrations, **(f)** Drain- and source widths, **(g)** Electron and hole mobility, **(h)** Gate-oxide layer thicknesses and **(i)** Metal-semiconductor contact types at a constant $V_d = 0.1$ V, while **(j)** Demonstrates the drain-to-source terminal current versus the drain voltage at different contact distances and **(k)** The drain-to-source terminal current versus the drain voltage at different gate voltages.

source voltages are supplied by TENG or a voltage source. The effects of gate and drain voltages are analyzed in simulations, and three working modes of MOS are considered: Cut-off, Triode, and Saturation. The detailed Finite Element Modeling and Modeling Assumptions can be found at Supplementary Note 2.

The input-output (I/O) characteristics of each component are individually analyzed by studying the impact of various structural parameters on the Drain-Source terminal current and voltage prior to combined (TENG-MOS-LED) device simulations in order to ensure maximum optical power emitted from the LED surface. For the triboelectric part, the gap distance between the triboelectric materials of the TENG operating in the contact-separation mode is varied, and the

corresponding output voltage at the TENG terminals is recorded. The gap distance is varied from 0 up to 8 μm during the stand-alone mode of the TENG operation. Secondly, the TENG terminals are coupled to the Gate-Source terminals of either the PMOS or the NMOS transistor type with the proper polarity. The effect of the gap distance between the triboelectric materials on the potential distribution around the gate substrate material is investigated for the NMOS and the PMOS transistor types. The MOSFET Gate-Source terminals are coupled to the two triboelectric materials via the Aluminum electrodes with the proper polarity. The Drain terminal of the MOSFET transistor is coupled either to one of the two triboelectric materials. In this mode, the voltage required to enable the MOSFET transistor is obtained from the TENG. In order to increase the sensitivity of the Drain-Source current, an independent voltage source, in the form of an external battery, is employed to contribute the control of the Drain-Source current by biasing the MOSFET transistor, via the Drain-Source voltage, prior to applying the Gate voltage via the TENG terminals. Two types of MOSFET transistor (PMOS and NMOS) are considered in order to analyze the performance of the electrons and holes. In order to investigate the transistor turn-on conditions and how much current it can transport, the I–V characteristics are plotted under a constant drain voltage of 0.1 V which is represented in Fig. 2. Firstly, the relationship between the gap distance between the two triboelectric materials and the potential distribution created around the gate layer for the two types of the MOSFET transistor is studied. As shown in Fig. 2(a) and **(b)**, the spatial distributions of potential across the gate layer for NMOS and PMOS transistors are studied respectively at different contact distances. By increasing the gap distance between the triboeletric contacts, the potential distribution is focused around the gate layer showing a proportional relationship for its value with the increase in the gap distance.

Secondly, the study is continuing to include the both types of MOSEFT, but this time for the resulting Drain-to-Source terminal current. The investigation is performed while keeping the structural design parameters, mentioned above, fixed. The impact of the channel length between the source and the drain terminals on the flow of Source-Drain current is investigated. It can be observed as in Fig. 2(c) that the D-S channel length balances the current flowing and the threshold voltage, which is the required voltage to turn the MOSFET transistor ON. Fig. 2 (d) shows the impact of the doping concentrations on the MOSFET output current which is used to control the output optical power of the LED component. The body concentration is then kept constant, and the drain/source concentrations are changed. The same methodology is followed in varying body concentration as shown in Fig. 2(e) while maintaining the value of the drain/source concentration then fixed. The impact of other parameters as the width of drain and source layers is also studied, in which we proved that the small variations, within the accepted design ranges, do not affect the values of terminal current as shown in Fig. 2(f). Also, the effect of hole and electron mobility is investigated in Fig. 2(g). The sixth parameter that we discuss is the gate oxide thickness effects on the output current. Variety of the thickness parameters are still ongoing for both NMOS and PMOS transistors, and the results are observed. The impact of varying the gate-oxide layer thickness, Fig. 2(h), is to balance the amount of current flowing and the threshold voltage. The next parameter for investigation is the metal-semiconductor contact type's effect on the output current. There are two types of contacts: Ohmic and Schottky, Fig. 2(i).

The Schottky type of contact yields diode behavior at the Gate-Aluminum contact whereas the Ohmic contact model leads to a resistive behavior. The impact of the drain voltage on the output current is also investigated at different contact distances and different gate voltages respectively as represented in Fig. 2(j) and (k). This study contains different sets of data for MOS types and TENG modes of operations since the drain and gate voltages are supplied either by TENG or by a voltage source.

The resulting Drain-Source current is applied to each of the LED terminal pairs individually. In order to analyze the material properties and quality, the same circumstances are applied to the three LED types. It can be observed that the threshold voltage for getting output optical power of the three LEDs types is about 3.5 V which corresponds to a contact distance of 0.7 μm. For contact distances corresponding to gate voltages between 0 and 2.4 V, the three LEDs are in their dead region and no significant emission is observed. Beyond 2.4 V, the three LEDs types show a piecewise linear relationship with the gate voltage. Fig. 3 (a), shows three different LEDs arrays powered using three TENGs. Furthermore, the emission rate with respect to voltage and terminal current is presented for the three LEDs as shown in Fig. 3(b)–(c). We observe that green and red LEDs have almost the same emission rates with different voltage and terminal current.

Although the three LED array in Fig. 3(a) appears to have a discontinuous structure and individually separated, this discontinuity in the geometrical configuration does not appear on the macroscopic scale. This small-scale arrangement leads to desirable color interference among the three emitted wavelengths such that new colors are generated when observed by a naked eye. Based on Fig. 3(b)–(c), it is noted that optical emissions within the proposed structure are less sensitive to the variations in the input TENG voltage than the drain-source current. Optical emissions at TENG voltages from 0 V to about 2.4 V are nearly negligible. This region can be viewed as the voltage dead region of the TENG-MOSFET-LED structure.

However, the output optical intensity varies rapidly with TENG voltages between 2.4 V up to 3.5 V. Meanwhile, a noticeable rapid increase of the output optical intensity as the drain-source current is increased from 0 to about 0.5 mA. The optical intensity shows a piecewise linear increase with the drain-source current beyond 0.5 mA. These observations are true for the three LED types and emphasize the role of the MOSFET transistor to interface the TENG-LED configuration. From a macroscopic viewpoint, the potential difference between the TENG electrodes due to their opposite triboelectric charges could be rapidly discharged via the LED in the absence of the MOSFET transistor. Nevertheless, the optical emission might cease upon the rapid transient discharging time. From a microscopic viewpoint, optical emission processes are strongly influenced by the drift mobility of the charge carriers (i.e., electrons and holes) as forced radiative bandgap transitions by these charge carriers are stimulated by their mutual collisions while drifting across the heterojunction structure.

It is well known from the image processing theory that more colors, which do not exist in the visible band of the spectrum but still visible to the human eye, can be obtained by linearly combining the optical powers of the three basic colors, namely, red, green and blue. The resulting effective color is determined by the set of the powers $(P_o^{(R)}, P_o^{(G)}, P_o^{(B)})$ emitted wavelengths $(\lambda_o^{(R)}, \lambda_o^{(G)}, \lambda_o^{(B)})$. Based on the value of $I_{LED}^{(i)}$, there exists an infinite continuous set of colors, usually known as the color space. Since the output optical power set $(P_o^{(R)}, P_o^{(G)}, P_o^{(B)})$ is a continuous variable of the input gate voltage (or equivalently the TENG contact distance). However, a quantized finite color subset can be obtained by quantization of the input gate voltage. In this context, each of the color intensities $(P_o^{(R)}, P_o^{(G)}, P_o^{(B)})$ is mapped to the corresponding quantized finite set $(L^{(R)}, L^{(G)}, L^{(B)}); L_q^{(i)} \in \{L_0^{(i)}, L_1^{(i)}, ..., L_7^{(i)}\}$, where $L_q^{(i)} = \frac{q}{2^n} I_{LED}^{(i)}(V_{DD} - V_{DS}); q = \sum_{j=0}^{n-1} b_j^{(i)} 2^j, q \in \{0, 1, ..., M\}$ $M = 2^n$-1and n is the order of the encoder, measured in binary digits (bits), see Table S3.

Accordingly, the quantized set $(L^{(R)}, L^{(G)}, L^{(B)})$ results in $8 \times 8 \times 8 = 512$ color combinations. Fig. 3(d)–(h) depicts the relationship between L_R, L_G, L_B and the TENG voltage. These voltages correspond to eight values of contact distances. This set is generated and verified through simulations by applying the three sets, each of 3-bits to the input of binary encoders with the output of each encoder is then forwarded to the input of the corresponding LED. The emitted optical intensity of each LED is, therefore, a quantized set of eight values and corresponds to an input TENG voltage from 0 to 3.5 V through steps of 0.5 V. This is to be consistent to the digital levels of the MOSFET technology. These discrete

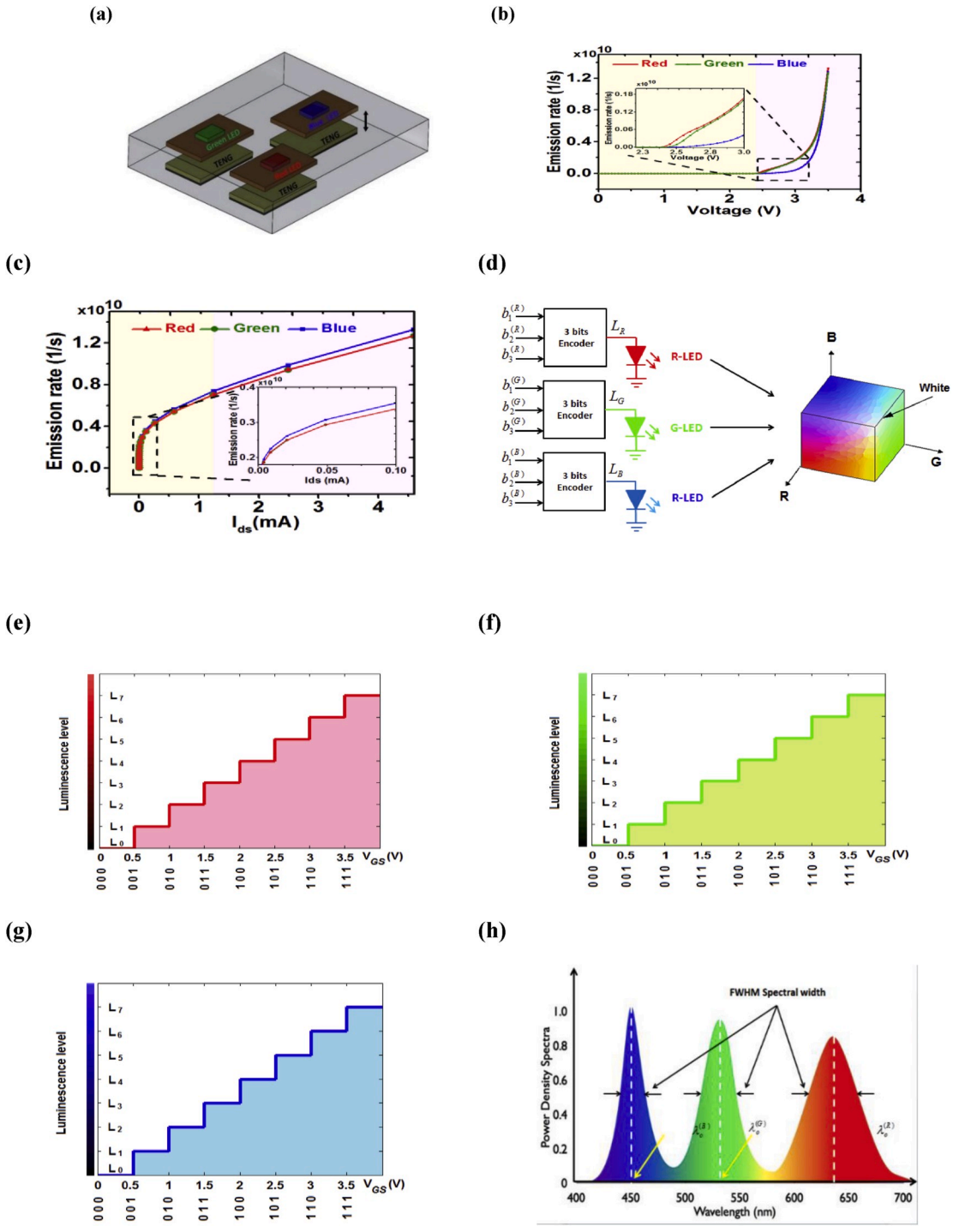

Fig. 3. (a) Principle of operation of the TENG controlled monochromatic pixel through the MOSFET transistor with three LED with different colors. The drain-source terminal current of the (b) Red LED, Green LED, and Blue LED at different values of the gate voltage supplied by the triboelectric generator. The normalized spontaneous emission spectrum of the (c) RED LED, Green LED, and Blue LED at different values of the drain-source terminal current which is controlled by the gate voltage supplied by the triboelectric generator. (d) Schematic configuration of the 3-bits binary encoders and the output optical intensity versus the TENG drive voltage at the gate-source terminal along with the binary equivalent code for (e) Red LED (f) Green LED and (g) Blue LED. (h) Normalized output optical power spectral density at the three emitted basic colors.

voltage values of the input gate voltage are the output of a 3-bit binary encoder as depicted in Fig. 3(d). Table S4 illustrates eight selected colors, among 512 available, along with their combinations $(L^{(R)}, L^{(G)}, L^{(B)})$ and encoding bits.

Fig. 4 represents the optical characterization for Blue LED under forwarding bias conditions. The emission spectra of the InGaN/GaN LED are observed at different values of the electrical forward bias conditions in Fig. 4(a). The forward bias voltage varies from 0 V to 3.5 V. Fig. 4(b) depicts the energy band diagrams for the conduction band energy level (E_c), the electron-quasi-Fermi energy level (E_{fn}), the hole-quasi-Fermi energy level (E_{fp}) and valence band energy level (E_v) versus the heterojunction length, denoted by Z and measured in μm at the same forward bias conditions in Fig. 4(a). Fig. 4(c) presents the carrier concentration for electron and hole across the junction length Z. The spatial

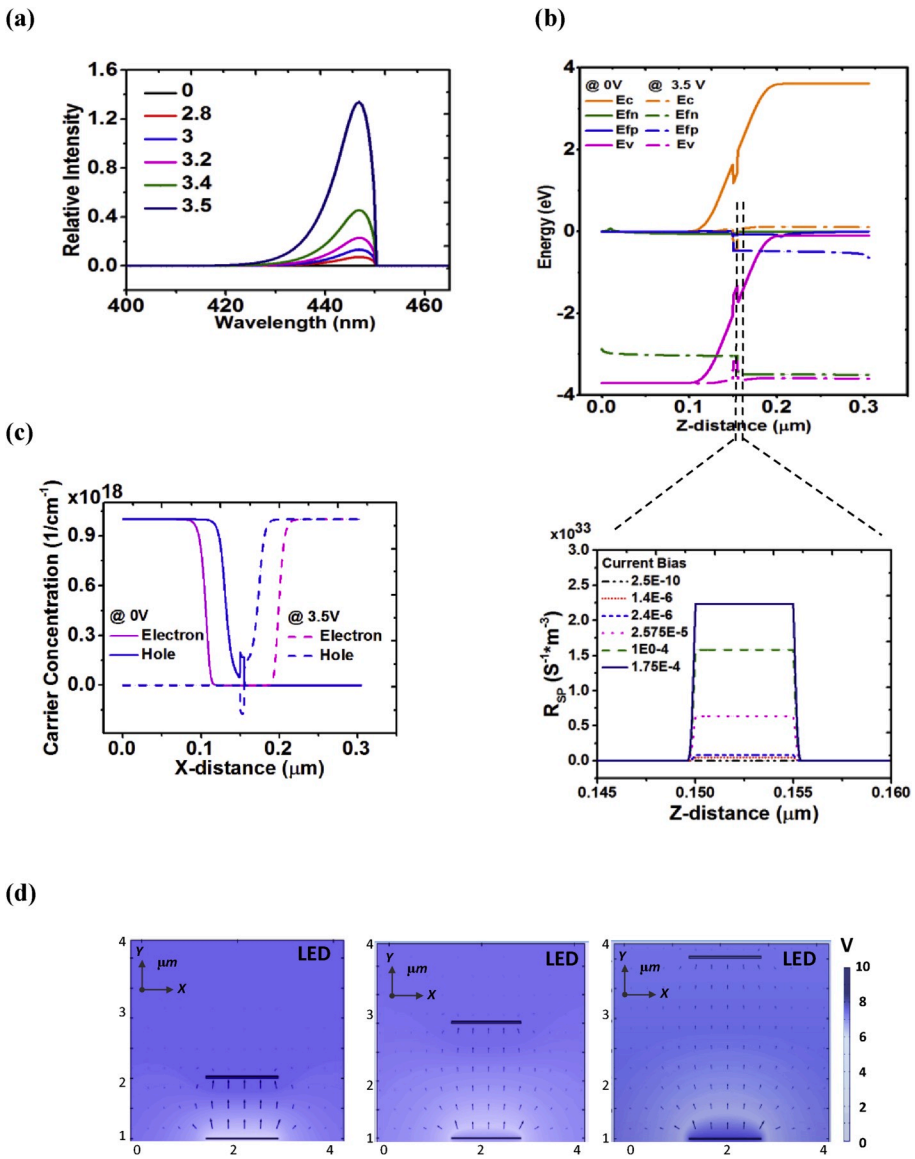

Fig. 4. (a) Relative intensity of emission versus the emission wavelength for Blue LED, each at different values of the gate voltage supplied by the triboelectric generator ranging from 0 up to 3.5 V. **(b)** Energy band diagrams corresponding to each bias voltage for the Blue LED, inset, spontaneous emission recombination rate ($m^{-3}S^{-1}$) versus z distance at different current bias **(c)** The variation of the carrier concentration versus the junction length for the Blue LED. **(d)** Light emission intensity of the Blue LED under different contact distance.

distribution of the emission rate around the hetero-structure junction is presented in Fig. 4(d).

As conduction band electrons in n-GaN and valence band holes in p-GaN are injected into InGaN/GaN region, both charge carrier types fall into the vacancy positions resulting in blue energy photons due to radiative recombinations. The peak radiated power spectral density increases as the TENG voltage increased from 0 V to 3.5 V indicating an electro-optic conversion process. In addition, a blue-shift of luminescence peak is observed with the increase of the applied TENG voltage. Fig. 4(b) illustrates the energy band diagrams corresponding to the extreme bias voltages of 0 V and 3.5 V.

In addition, spontaneous emission recombination rate R_{sp} versus the hetero-junction length Z at different current bias is calculated as shown in Fig. 4(b) inset. The R_{sp} increases as the current bias is increased. We observe that the emission rate increases as the contact distance between the tribo layers is increased. The increase in the optical emission rate is attributed to the forward bias voltage whose role is to lower the energy barrier between the corresponding energy levels at the two sides of the heterostructure junction. This reduction in the energy band difference allows more kinetically energized charge carriers to easily cross the junction. Moreover, it can be observed from Fig. 4(b) that remarkable emissions take place over only 5 nm of the junction width. Electroluminescence results are strongly influenced by the geometrical design of the active region.

Fig. 5 presents the relative intensity and energy band level of the other two LEDs (green and red). As shown in Fig. 5(a), the maximum relative intensity occurs at a maximum voltage of 3.5 V and equals approximately 0.4, and this happens at a wavelength of 680 nm for the Red LED. Meanwhile, this relative peak intensity happens for the Green LED at a wavelength of 525 nm and the intensity peak reaches 0.8 at a voltage of 3.5 V. Furthermore, the energy band level for green and red LEDs are illustrated in Fig. 5(c), (d). Fig. 5(e) demonstrates the variation of the photo-excitation current with the gap distance between the two triboelectric materials at different values of the drain voltage. The corresponding spontaneous emission rate resulting from the radiative recombination of the injected carriers is illustrated in Fig. 5(f). The drain voltage is increased from 0 V to 5 V in small increments. The gate voltage is increased from 2 V to 5 V through 1 V step increments.

It can be observed that the spontaneous emission rate for the Green and Red LEDs is less than that produced by a Blue LED. This difference in the relative optical intensity could affect the resulting color map if not correctly adjusted. The surface in Fig. 5(e) indicates both the output optical intensity as well as the resulting color as seen by a human eye.

At low contact distances and drain voltage, optical emission of the

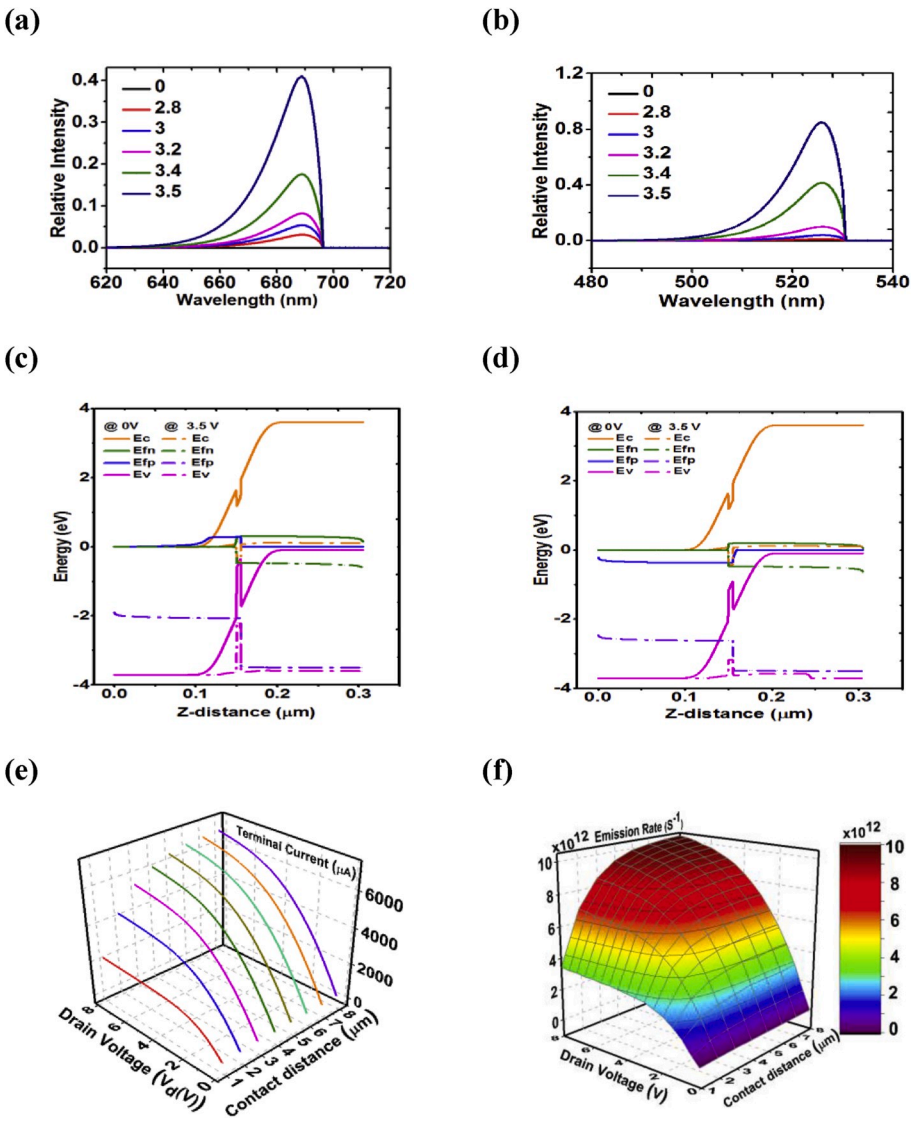

Fig. 5. Relative intensity of emission versus the emission wavelength for the **(a)** RED LED and **(b)** Green LED, each at different values of the gate voltage supplied by the triboelectric generator ranging from 0 up to 3.5 V. Energy band diagrams corresponding to each bias voltage for the **(c)** Red LED and **(d)** Green LED. **(e)** Variation of the photoexcitation current with the gap distance between the two triboelectric materials at different values of the drain voltage and **(f)** The overall RGB emission rate versus the contact distance and the drain voltage with the equivalent color and its intensity resulting from the radiative recombination of the injected carriers in the three LED configurations simultaneously.

Blue LED dominates the resulting optical power. Green and Red LEDs emissions seem to be less sensitive to the variation of these two control parameters. However, as the drain voltage and the TENG gap distance are increased towards their maximum values emission from the Green LED begins to dominate the resulting color. As these two control parameters reach their peak values, Red LED emission dominates the resulting color. This simultaneous variation of the three colors practically covers the whole visible spectrum.

The external electrical-to-optical efficiency η_i of the RGB LED device is investigated in order to assess its optical emission performance. The spontaneous emission rate-wavelength relationships are also evaluated. Fig. 5(f) shows the normalized spontaneous emission spectrum of the RGB LED device at different values of the drain-source current. This current is controlled by the gate voltage supplied by the triboelectric generator. It should be observed in Fig. S2 that around a zero-current density, the external quantum efficiency approaches to around 26% and then decreases drastically with the photo-excitation current density.

3. Conclusion

In summary, we have proposed a tribo-phototronic-based device by coupling a microstructure TENG to a LED via a MOSFET transistor. A comprehensive analysis is introduced and applied to the proposed device on the microstructure level and verified by simulations. This analysis can be generalized to many of phototronic-based devices. Simulation results further provide a deep understanding of the influence of the geometrical microstructural parameters on the carrier transportation processes in semiconductor devices. Following this methodology, we also study the effect of these structural parameters on the optical emission processes. Furthermore, we have shown that spontaneously emitted light can be extracted from an InGaN -based LED and can be mechanically controlled by interfacing a MOSFET transistor to the LED-TENG configuration whose role is to regulate photoexcitation current and the radiative processes of the LED. The impact of the structural and terminal parameters on the emitted optical power levels and color is investigated. It can be correctly included that, integrating arrays of the proposed device can offer a flexible, low-cost approach for potential applications of LEDs as used for displays, imaging, sensing, and communication.

Declaration of competing interest

The authors declare that they have no known competing financial interests or personal relationships that could have appeared to influence the work reported in this paper.

CRediT authorship contribution statement

Abdelsalam Ahmed: Conceptualization, Writing - original draft, Writing - review & editing, Supervision. **Mohamed Shehata:** Conceptualization, Writing - original draft, Writing - review & editing. **Islam Hassan:** Writing - original draft, Writing - review & editing. **Yasmine I. Abdelhak:** Writing - review & editing. **Efe Cigdem:** Formal analysis, Methodology. **Maher El-Kady:** Writing - review & editing. **Yehea Ismail:** Writing - review & editing, Supervision. **Hassan Mostafa:** Conceptualization, Writing - review & editing, Supervision.

Appendix A. Supplementary data

Supplementary data to this article can be found online at https://doi.org/10.1016/j.nanoen.2020.104874.

References

[1] F.R. Fan, Z.Q. Tian, Z.L. Wang, Nano Energy (2012), https://doi.org/10.1016/j.nanoen.2012.01.004.
[2] G. Zhu, Z.-H. Lin, Q. Jing, P. Bai, C. Pan, Y. Yang, Y. Zhou, Z.L. Wang, Nano Lett. 13 (2013) 847–853.
[3] F. Fan, Z. Tian, Z.L. Wang, Nanophotonics, Nanoelectronics and Nanosensor, Optical Society of America, 2013. NSa3A. 17.
[4] Z.L. Wang, ACS Nano 7 (2013) 9533–9557.
[5] M.F. El-Kady, A. Ahmed, I. Hassan, A. Negm, A.M. Pourrahimi, M. Muni, et al., Fire-retardant, self-extinguishing triboelectric nanogenerators, Nano Energy 59 (2019) 336–345.
[6] A. Ahmed, I. Hassan, M. Hedaya, T.A. El-Yazid, J. Zu, Z.L. Wang, Nano Energy 36 (2017) 21–29.
[7] A. Ahmed, I. Hassan, T. Ibn-Mohammed, H. Mostafa, I.M. Reaney, L.S. Koh, J. Zu, Z.L. Wang, Energy Environ. Sci. 10 (2017) 653–671.
[8] A. Ahmed, I. Hassan, T. Jiang, K. Youssef, L. Liu, M. Hedaya, T.A. Yazid, J. Zu, Z. L. Wang, Nanotechnology 28 (2017) 185403.
[9] A. Ahmed, I. Hassan, I.M. Mosa, E. Elsanadidy, G.S. Phadke, M.F. El-Kady, J. F. Rusling, P.R. Selvaganapathy, R.B. Kaner, Nano Energy 60 (2019) 17–25.
[10] A. Ahmed, I. Hassan, I.M. Mosa, E. Elsanadidy, M. Sharafeldin, J.F. Rusling, S. Ren, Adv. Mater. (2019) 1807201.
[11] A. Ahmed, I. Hassan, P. Song, M. Gamaleldin, A. Radhi, N. Panwar, S.C. Tjin, A. Y. Desoky, D. Sinton, K.-T. Yong, J. Zu, Sci. Rep. 7 (2017) 17143.
[12] A. Ahmed, I. Hassan, J. Zu, Adv. Eng. Mater. (2018) 1700997.
[13] A. Ahmed, Z. Saadatnia, I. Hassan, Y. Zi, Y. Xi, X. He, J. Zu, Z.L. Wang, Adv. Energy Mater. 7 (2017).
[14] A. Ahmed, S.L. Zhang, I. Hassan, Z. Saadatnia, Y. Zi, J. Zu, Z.L. Wang, Extreme Mech. Lett. 13 (2017) 25–35.
[15] C. Zhang, Z.L. Wang, Nano Today 11 (2016) 521–536.
[16] W. Peng, R. Yu, Y. He, Z.L. Wang, ACS Nano 10 (2016) 4395–4402.
[17] C. Zhang, L.M. Zhang, W. Tang, C.B. Han, Z.L. Wang, Adv. Mater. 27 (2015) 3533–3540.
[18] Y. Pang, J. Li, T. Zhou, Z. Yang, J. Luo, L. Zhang, G. Dong, C. Zhang, Z.L. Wang, Nano Energy 31 (2017) 533–540.
[19] Y. Liu, S. Niu, Z.L. Wang, Adv. Electron. Mater. 1 (2015) 1500124.
[20] J. Li, C. Zhang, L. Duan, L.M. Zhang, L.D. Wang, G.F. Dong, Z.L. Wang, Adv. Mater. 28 (2016) 106–110.
[21] B.-U. Hwang, J.-H. Lee, T.Q. Trung, E. Roh, D.-I. Kim, S.-W. Kim, N.-E. Lee, ACS Nano 9 (2015) 8801–8810.
[22] C. Zhang, W. Tang, L. Zhang, C. Han, Z.L. Wang, ACS Nano 8 (2014) 8702–8709.
[23] F. Xue, L. Chen, L. Wang, Y. Pang, J. Chen, C. Zhang, Z.L. Wang, Adv. Funct. Mater. 26 (2016) 2104–2109.
[24] Z.W. Yang, Y. Pang, L. Zhang, C. Lu, J. Chen, T. Zhou, C. Zhang, Z.L. Wang, ACS Nano 10 (2016) 10912–10920.
[25] C. Zhang, J. Li, C.B. Han, L.M. Zhang, X.Y. Chen, L.D. Wang, G.F. Dong, Z.L. Wang, Adv. Funct. Mater. 25 (2015) 5625–5632.
[26] B.H. Kim, S. Nam, N. Oh, S.-Y. Cho, K.J. Yu, C.H. Lee, J. Zhang, K. Deshpande, P. Trefonas, J.-H. Kim, ACS Nano 10 (2016) 4920–4925.
[27] M. Peng, Y. Zhang, Y. Liu, M. Song, J. Zhai, Z.L. Wang, Adv. Mater. 26 (2014) 6767–6772.
[28] T. Zhou, Z.W. Yang, Y. Pang, L. Xu, C. Zhang, Z.L. Wang, ACS Nano 11 (2017) 882–888.
[29] Y. Pang, F. Xue, L. Wang, J. Chen, J. Luo, T. Jiang, C. Zhang, Z.L. Wang, Adv. Sci. 3 (2016) 1500419.
[30] C. Zhang, Z.H. Zhang, X. Yang, T. Zhou, C.B. Han, Z.L. Wang, Adv. Funct. Mater. 26 (2016) 2554–2560.